Geometrical and transport properties of random packings of polydisperse spheres

V. Mourzenko* and J.-F. Thovert†
LCD, SP2MI, Boîte Postale 30179, 86962 Futuroscope Cedex, France

O. Vizika‡
Institut Français du Pétrole (IFP), 1 et 4, avenue de Bois-Préau, 92852 Rueil-Malmaison Cedex, France

P. M. Adler§
UPMC Sisyphe, Boîte 105, 4 place Jussieu, 75252 Paris Cedex 05, France
(Received 17 January 2008; published 11 June 2008)

Loose packings of spheres with bidisperse or log-normal distributions are generated by random sequential deposition. Porosity, conductivity, and permeability are determined. The porosities correspond to loose packings, but they follow the usual trends for bidisperse packings. The conductivity and permeability follow power laws as functions of the porosity of the packings. Several other quantities such as the classical Kozeny constant are successfully represented as functions of porosity. Some dimensionless representations gather the numerical data on curves valid for all particle distributions. Finally, comparisons with experimental data are satisfactory.

DOI: 10.1103/PhysRevE.77.066306 PACS number(s): 47.56.+r, 81.05.Rm, 41.20.Cv

I. INTRODUCTION

Grain packings have given rise to a considerable interest for a long time, as a model for various types of porous media such as geological materials like soils. Of course, regular packings have been extensively studied, since their simple geometries make an analytical or semianalytical determination of their properties achievable. However, they do not account for the random character of most natural media. Therefore, we shall not dwell on these models, and focus rather on three-dimensional random packings and on their macroscopic properties such as conductivity and permeability.

A considerable literature has accumulated over the years on this topic. A few surveys [1–5] review most of the works done before 1990. The following brief survey will concentrate on the recent contributions and it will address the numerical generation, the theoretical analysis, the determination of the macroscopic properties of packings, and the experiments on packings.

Two major kinds of methods are used to generate random packings, namely, random sequential addition and collective rearrangement. The two methods can mimic the physical processes which generate real particle packings, such as deposition by gravity for the first one while the second one is closer to generation of packings by shaking. The first method usually generates packings with a larger porosity than collective rearrangement.

For sake of completeness, it may be interesting to mention various techniques of collective rearrangement such as that described in [6]: the particles that initially have random positions and may overlap are moved in order to suppress the overlaps and they grow in order to reduce porosity. Similar techniques are given in [7] and [8]. Kansal *et al.* [9] used a nonequilibrium molecular dynamics simulation in which the spheres grow over time; the growth rate of a sphere is proportional to its initial diameter. Kristiansen *et al.* [10] used a mechanical contraction technique similar to [8]; the particles are distributed at random in a large cell which is contracted repeatedly in steps; in each step, the overlaps are removed by relocating the particles. The cell is contracted until the overlaps can no longer be removed.

Random sequential addition has been less used recently though it has the advantage of mimicking deposition by gravity. In a ballistic deposition such as in the pioneering work of Vold [11], the grain trajectories toward their final positions are built explicitly, which ensures that a particle can actually reach its position during the genesis of the packing. This technique was extended to star particles by Coelho *et al.* [12], who surveyed extensively the literature prior to 1997. The macroscopic conductivity, the permeability, and the dispersion were systematically determined in [12]. Moreover, the properties of these monodisperse packings were studied in a series of other publications such as [13] for application to NMR. Santiso and Müller [14] used a similar algorithm though limited to spheres. The novel feature is that several tries are made for each settling particle and the one that provides the lowest position is retained; for monodisperse spheres, the porosity is not significantly smaller than the one obtained in [12].

Recent theoretical studies predicting the properties of polydisperse sphere packings are scarce. Yu and Standish [15,16] devised a semiempirical fit of the experimental results. For a given ratio of radii, there exists a fraction of the small particles for which the overall porosity of a bidisperse packing is minimal; this fraction and the corresponding porosity can be approximated by relations derived from former experiments; then, a sort of interpolation is proposed between this minimal porosity and the maximal porosity which corresponds to monodisperse packings. It should be noticed that this semiempirical approach is quite successful since it

*murzenko@lcd.ensma.fr
†thovert@lcd.ensma.fr
‡Olga.VIZIKA-KAVVADIAS@ifp.fr
§pierre.adler@upmc.fr

compares well with many numerical simulations [7,8]. Patlazhan [17] used a statistical geometrical approach by dividing a random packing of hard spheres into a set of tetrahedra with the vertices coinciding with the centers of the neighboring particles. Then spheres of different types are distributed at random in these tetrahedra.

Finally, some recent investigations which are at least partly experimental should be mentioned. The permeability of binary silica sphere packings was experimentally determined and successfully compared to the classical Kozeny-Carman relation in [18]. Studies of a more applied nature were carried out in packings inside cylindrical tubes in [19]. Two-phase gas-solid flow through packed beds was studied in [20]. Finally, the review of [21] about dispersion in packed beds is of general interest.

This paper has two major objectives. First, it is a continuation of [12]; it aims to obtain more precise numerical results for the macroscopic properties of monodisperse packings of spheres such as conductivity and permeability, thanks to the development of computational power during the last ten years. Second, it extends the results of [12] to bidisperse and polydisperse packings of spheres in a systematic way. Therefore, this paper is focused more on the transport properties of the packings than on the packings themselves.

The paper is organized as follows. Section II recalls briefly the sequential deposition algorithm of [12]. Then, the major parameters used in the numerical simulations are summarized; here again the reader is referred to [12] for a complete account of the necessary parameters. Section III is devoted to a brief description of the main geometric and transport properties, which are systematically calculated and to the necessary methodology to calculate them. Results are presented and discussed in Secs. IV and V. The porosities of bidisperse and log-normal packings which are obtained with the algorithm of [12] are presented in Sec. IV and briefly compared to the literature data. The major emphasis is put on Sec. V, where the conductivity and permeability are systematically calculated for these two types of packing. It is important to notice that a major effort has been made in order to obtain precise numerical data, i.e., in the limit of a very precise discretization of geometry.

II. CONSTRUCTION OF RANDOM PACKINGS

A. Sequential deposition algorithm

Our random packings result from the successive deposition of grains in a "gravitational" field. The grains are introduced at a random location above the bed already in place, and fall until they reach a local minimum of their potential energy. Sometimes, a dynamic language is used, but the reader should not be misled, since Newton's laws of motion are never solved. During their fall, any displacement and rotation that contribute to lowering their barycenter are allowed.

As a general rule, a mobile particle is allowed to slip freely on the bed surface as long as the elevation of the barycenter can be diminished. Morever, each elementary displacement of a grain is independent of its previous position and orientation increments. However, as described below, an adjustable parameter favors either translation or rotation of the particle, when both motions could lower its elevation. Finally, the interactions are reduced to steric exclusion. A variant of this rule has been devised to simulate short-range attractive forces, which could create permanent links between grains. After contact, a settling grain can be allowed to rotate around the contact point without slip (but the contact may move if the grain rolls on the bed). For instance, for parallelepipedic grains, if a vertex comes in contact with an underlying plane solid surface, the particle will rotate until one of its edges and eventually one of its faces becomes tangent to this surface.

The novel feature of our algorithm was that each particle may have any size and shape, provided that it can be described in a spherical polar coordinate system (r,θ,ϕ) attached to it by a single-valued function $\rho(\theta,\phi)$. The inner volume of the particle is defined by

$$r \leq \rho(\theta,\phi). \tag{1}$$

Obviously, any convex particle shape can be described by (1). This paper only deals with spherical particles, but it could be easily extended to the shapes studied in [12].

The position of a particle is represented by the location $\boldsymbol{r}=(x,y,z)$ of its barycenter, and by a set ω of three angles that give the orientation of the particle with respect to the coordinate system. The z axis is oriented upward. The grains are deposited in a square vertical box, with a flat bottom at $z=0$, and periodicity conditions along the x and y directions in order to avoid the well-known hard-wall effects (see Fig. 2). Note that such hard-wall effects have been addressed by Ding *et al.* [20] and Mehta and Hawley [22].

TABLE I. List of radii used for the bidisperse packings.

ρ	2	3	4	5	6	8
r	2/3	1/2	2/5	2/5	2/5	2/5
R	4/3	3/2	8/5	10/5	12/5	16/5

B. Parameters of the numerical simulations

1. Definition of the grain size distributions

Two major types of packing are considered. First, bidisperse packings of spheres of radii r and R (with $r \leq R$) are generated according to the algorithm described in Sec. II A. The two radii are generally chosen in such a way that their average is equal to 1 in order to keep the same precision in the packing generation. The ratio R/r is denoted by ρ and the volume fraction of large grains by f_R. More precisely,

$$R = \frac{2\rho}{1+\rho}, \quad r = \frac{2}{1+\rho}. \tag{2}$$

However, when $\rho \geq 5$ and $f_R \leq 0.7$, the number of small grains that results from (2) becomes numerically overwhelming. Thus, in such cases, r was kept equal to 2/5, with $R = 2\rho/5$. Table I provides the list of radii used for bidisperse packings. f_R varies from 0 to 1 by steps equal to 0.1 and 0.2.

Second, polydisperse spheres with a log-normal distribution of the radius R are randomly packed. More precisely, the

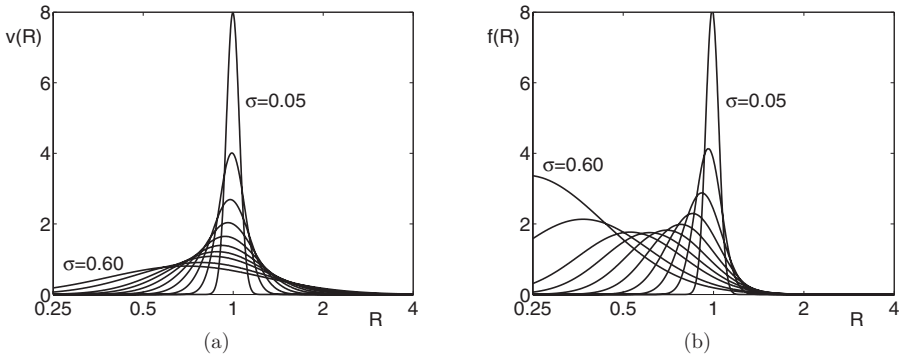

FIG. 1. Log-normal grain size distributions in volume (a) and in number (b). The standard deviation σ [cf. (3)] varies from 0.05 up to 0.40 in steps equal to 0.05; two larger values equal to 0.5 and 0.6 are also used. The lower and upper cuttoffs are given by $R_{\min}=0.25$ and $R_{\max}=4$, respectively; the distributions are renormalized accordingly.

grain size distributions in number $f(R)$ and in volume $v(R)$ are given by

$$v(R) = \frac{1}{\sqrt{2\pi}\sigma R}\exp\left(\frac{(\ln R - \mu)^2}{2\sigma^2}\right),$$

$$f(R) = \frac{\langle R^3\rangle}{\sqrt{2\pi}\sigma R^4}\exp\left(\frac{(\ln R - \mu)^2}{2\sigma^2}\right), \quad (3)$$

where μ is the average of the logarithm of the radius, and σ its standard deviation. Experimentally, real packings are mostly characterized by $v(R)$, but numerical packings are more easily generated with $f(R)$. In order to compare the various results, μ is always equal to 1. The standard deviation σ varies from 0.05 up to 0.40 by steps equal to 0.05; two larger values equal to 0.5 and 0.6 are also used. These distributions, which in principle go from 0 up to infinity, are limited by a smallest and a largest radius equal to $R_{\min}=0.25$ and $R_{\max}=4$, respectively. The values of v and f are renormalized accordingly in this interval. These distributions are illustrated in Fig. 1.

2. Overall dimensions of the samples

The packings are built by sequentially depositing particles in a "box" with a square $L\times L$ horizontal cross section (see Fig. 2) and a flat hard bottom. In order to minimize size effects, periodicity conditions are applied along the two horizontal directions. The height of the box is equal to $8L$. Deposition stops when a particle cannot enter totally into the cell.

The box is divided into ten layers of dimensions $L\times L\times 0.8L$. The bottom and the top layers are discarded and the calculations are performed on the eight intermediate layers. Results are averaged over these eight layers. In this paper, for bidisperse and log-normal populations, L is equal to 16 for an average radius equal to 1 in most cases. Therefore, the overall size of the cell is given by $16\times 16\times 128$.

3. Additional numerical remarks

The algorithm is controlled by seven parameters, and the influence of these parameters is detailed in [12] where additional information is given. Moreover, systematic studies on the statistical fluctuations were performed in [12]. Such statistical fluctuations were controlled here by examination of the porosity variations along the z axis. Except when segregation occurs (see Sec. IV), the statistical fluctuations are low. For instance, for bidisperse packings with $\rho=2$, the porosities in the ten slices of size $L\times L\times 0.8L$ depart by less than ± 0.005 from the global average. The influence of the flat bottom is limited to the first slice, which is systematically discarded from the calculations of the transport properties.

Finally, thanks to the increased computer speed, the generation of a packing is now much faster than reported in [12]. The computational cost depends greatly on the grain size distribution. The calculations are very fast for narrow distributions, when the grain trajectories involve generally only a few bounces. For instance, about 360 grains per second are deposited for a bidisperse population with $\rho=2$ and $f_R=0.70$. Broad distributions are more demanding. For example, about 13 grains are deposited per second for a log-normal distribution with $\sigma=0.5$. Theses rates are given for a 1.2 GHz Power5 RISC processor. However, in all cases the packing generation is fast compared to the subsequent simulations for the characterization of its transport properties.

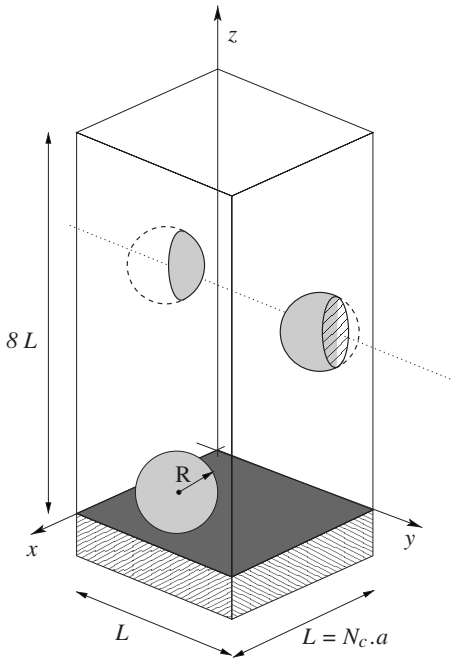

FIG. 2. Schematic diagram of the unit cell with periodic boundary conditions; illustration of some geometrical notations.

III. MACROSCOPIC PROPERTIES

A. Geometric properties

Since in this paper spherical particles are addressed, only overall scalar parameters can be introduced. Let V_p and S_p denote the pore volume and the surface of the solid interface, respectively. According to standard definitions [23], the hydraulic radius R_H is defined as the ratio of the total pore volume to its surface area,

$$R_H = \frac{V_p}{S_p}. \tag{4}$$

An equivalent radius $\tilde{R}$ can be defined as the inverse of the harmonic mean radius,

$$\tilde{R} = \left(\int \frac{v(R)dR}{R} \right)^{-1}, \tag{5a}$$

where $v(R)$ is the probability density in volume [cf. (3)]. $\tilde{R}$ has interesting properties since it can also be written as

$$\tilde{R} = \frac{\int R^3 f(R) dR}{\int R^2 f(R) dR} \tag{5b}$$

and as

$$\tilde{R} = \frac{\int 4\pi R^2 f(R) R \, dR}{\int 4\pi R^2 f(R) dR}. \tag{5c}$$

In the last expression, the average is weighted by the sphere surfaces.

Another property is worth mentioning. Whatever the radius distribution, the following relation holds for spheres:

$$R_H = \frac{\epsilon}{3(1-\epsilon)} \tilde{R}. \tag{6}$$

Therefore, two sphere packings with the same porosity and the same $\tilde{R}$ have the same hydraulic radius and the same surface area of the pores, whatever the radius distribution.

These quantities can be determined on the packings generated by the algorithm since the coordinates of the sphere centers and the sphere radii are recorded. The spheres whose centers are located between two horizontal planes are known; the total solid volume and the total solid interface can be readily deduced.

Another possible way consists in discretizing the spheres and then performing the previous measurements on the discretized array. More precisely, space is discretized into $N_{cx} \times N_{cy} \times N_{cz}$ elementary cubes of size a; generally, $N_{cx}=N_{cy}$. Whenever the center of an elementary cube falls in the solid (fluid) phase, the whole cube is considered as filled with solid (fluid). Note that the transport calculations are done on these discretized arrays.

It is easy to realize that volumes are relatively insensitive to the way they are measured, but this is not the case for surfaces, where a systematic bias is present. More precisely, numerical evaluations of isotropic surfaces are overestimated by a factor 3/2 by the discrete numerical scheme used here. However, this effect is partly compensated by the nonzero area of the grain contacts in the discretized representation, which lowers the wetted area. (6) is compared to the numerical data in Fig. 3 where the mean grain radius is $10a$. Note that in this comparison $\tilde{R}$ is derived from (4) while the numerical value of S_p is deduced from the spatial correlation of the pore phase function determined on the discretized packings (see [23]). Accordingly, the numerical data are almost underestimated by a factor 2/3; the difference is due to the contacts between spheres, whose influence decreases when ρ increases.

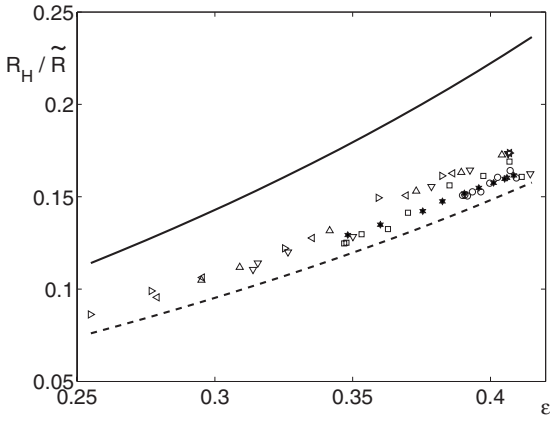

FIG. 3. Ratio of the hydraulic radius R_H and the equivalent radius $\tilde{R}$. The solid line corresponds to (6), and the broken line to 2/3 of (6). The symbols correspond to bidisperse packings with $f_R=0$ to 1 and $\rho=2$ (○), 3 (□), 4 (▽), 5 (△), 6 (◁), and 8 (▷), and to log-normal packings with σ up to 0.6 (★) when the mean grain radius is $10a$.

B. Transport properties

In this section, the macroscopic effective coefficients for the basic transport processes by conduction and convection in random packed beds are determined. The governing equations and their methods of solution are briefly recalled in this section. In all cases, the macroscopic coefficients are deduced by integrating the local fields, obtained by solving the transport equations at the pore scale.

Since the packings are macroscopically homogeneous, they are considered as infinite periodic media, made of identical unit cells. Note that the packings are indeed built with periodic conditions along the two horizontal directions. However, when a cubic sample is cut from a deposited bed, the lower and upper faces do not match each other. This may affect the computation of the transport properties along the vertical axis. The content of a unit cell is discretized into $N_{cx} \times N_{cy} \times N_{cz}$ elementary cubes of size a as mentioned above. In this paper, one has $N_c=N_{cx}=N_{cy}=1.25N_{cz}$. Therefore, the horizontal sides of the unit cell are $L=N_{cx}a$. The volume of the unit cell is denoted by τ_0 and its outer surface by $\partial\tau_0$.

Since the values of N_c differ from case to case, they will be given when appropriate. However, the value $N_c=160$ is commonly used which means that the unit scale is equal to $10a$. When discretization effects are studied, the values $N_c=128$, 160, 192, and 256 are used.

1. Conduction

The electrical terminology is used here, but the following developments are also valid for thermal conduction and for diffusion of Brownian particles whose size is small with respect to a typical size of the medium. The local flux $\boldsymbol{q}$ is equal to

$$\boldsymbol{q} = -\Sigma_0 \boldsymbol{\nabla} \psi, \tag{7}$$

where Σ_0 is the fluid conductivity. Electrical and thermal conduction are both governed by a Laplace equation ([24] and [23] where additional details are given), which corresponds to the conservation of the local electrical flux,

$$\nabla^2 \psi = 0, \tag{8}$$

where ψ is the local electrical potential, together with the no-flux boundary condition at the wall S_p when the solid phase is assumed to be insulating,

$$\boldsymbol{n} \cdot \boldsymbol{\nabla} \psi = 0 \quad \text{on } S_p, \tag{9}$$

where $\boldsymbol{n}$ is the unit vector normal to S_p.

$\boldsymbol{\nabla}\psi$ is assumed to be spatially periodic with a period aN_c in the three directions of space. In addition, either the macroscopic potential gradient or the average electrical flux

$$\overline{\boldsymbol{q}} = \frac{1}{\tau_0} \int_{\partial \tau_0} \boldsymbol{R}\boldsymbol{q} \cdot d\boldsymbol{s} \tag{10}$$

is specified. These two quantities are related by the symmetric positive definite conductivity tensor $\boldsymbol{\Sigma}$

$$\overline{\boldsymbol{q}} = -\boldsymbol{\Sigma} \cdot \boldsymbol{\nabla} \psi, \tag{11}$$

which depends only upon the geometry of the medium.

On average, for an isotropic random medium, $\boldsymbol{\Sigma}$ is a spherical tensor equal to $\Sigma \cdot \boldsymbol{I}$. For deposited packings, the x and y directions play equivalent roles, but one may expect a different behavior along the z axis. In the following, for the sake of simplicity, Σ denotes the average of the conductivities along the x and y axes, which were indeed always found equal within statistical fluctuations.

The Neumann problem (8)–(10) is solved via a second-order finite-difference formulation. A conjugate-gradient method turned out to be very effective for the problem at hand, primarily because it is better suited to vectorial programming than implicit relaxation schemes.

The formation factor F is generally defined as the inverse of the dimensionless macroscopic conductivity,

$$F = \frac{\Sigma_0}{\Sigma}. \tag{12}$$

The length scale Λ defined by [25] can be used in order to characterize porous media. Λ is essentially a volume-to-surface pore ratio with a measure weighted by the local value of the electric field $\mathbf{E}(\mathbf{x})$ in a conduction process,

$$\Lambda = 2 \frac{\int_{V_p} |\mathbf{E}(\mathbf{x})|^2 dv}{\int_{S_p} |\mathbf{E}(\mathbf{x})|^2 ds}. \tag{13}$$

This quantity can be calculated when the Laplace equation (8) is solved in order to derive $\boldsymbol{\Sigma}$.

2. Stokes flow

The low-Reynolds-number flow of an incompressible Newtonian fluid is governed by the usual Stokes equations

$$\boldsymbol{\nabla} p = \mu_f \nabla^2 \boldsymbol{v}, \quad \boldsymbol{\nabla} \cdot \boldsymbol{v} = 0, \tag{14}$$

where $\boldsymbol{v}$, p, and μ_f are the velocity, pressure, and viscosity of the fluid, respectively. In general, $\boldsymbol{v}$ satisfies the no-slip condition at the wall,

$$\boldsymbol{v} = \boldsymbol{0} \quad \text{on } S_p. \tag{15a}$$

Because of the spatial periodicity of the medium, it can be shown ([26,23]) that $\boldsymbol{v}$ possesses the following property:

$$\boldsymbol{v} \text{ is spatially periodic along the three directions of space.} \tag{15b}$$

This system of equations and conditions applies locally at each point $\boldsymbol{R}$ of the interstitial fluid. In addition, it is assumed that either the seepage velocity vector is specified, i.e.,

$$\overline{\boldsymbol{v}} = \frac{1}{\tau_0} \int_{\partial \tau_0} \boldsymbol{R}\boldsymbol{v} \cdot d\boldsymbol{s} = \text{a prescribed constant vector}, \tag{16a}$$

or else the macroscopic pressure gradient is specified,

$$\overline{\boldsymbol{\nabla} p} = \text{a prescribed constant vector}. \tag{16b}$$

Note that (16) is easily derived from the identity valid for an incompressible fluid $\boldsymbol{v} = \boldsymbol{\nabla} \cdot (\boldsymbol{R}\boldsymbol{v})$ (cf. [23]). Since the system (14)–(16) is linear, it can be shown that $\overline{\boldsymbol{v}}$ is a linear function of $\overline{\boldsymbol{\nabla} p}$. These two quantities are related by the permeability tensor $\boldsymbol{K}$ such that

$$\overline{\boldsymbol{v}} = -\frac{1}{\mu_f} \boldsymbol{K} \cdot \boldsymbol{\nabla} p. \tag{17}$$

Here, $\boldsymbol{K}$ is a symmetric tensor that is positive definite. It depends only on the geometry of the system and thus can be simplified when the porous medium possesses geometric symmetries. Its diagonal component K_{xx} was calculated by imposing $\overline{\boldsymbol{\nabla} p}$ along the x axis. It is simply denoted by K in the following.

The numerical method that is used here is a second-order finite-difference scheme identical to the one first described in [26]. In order to cope with the continuity equation, the so-called artificial compressibility method was applied with a staggered marker-and-cell mesh [27].

The length scale Λ was proved to be very useful in many ways. As suggested by [25], [28] showed that the permeability K can be determined via Λ,

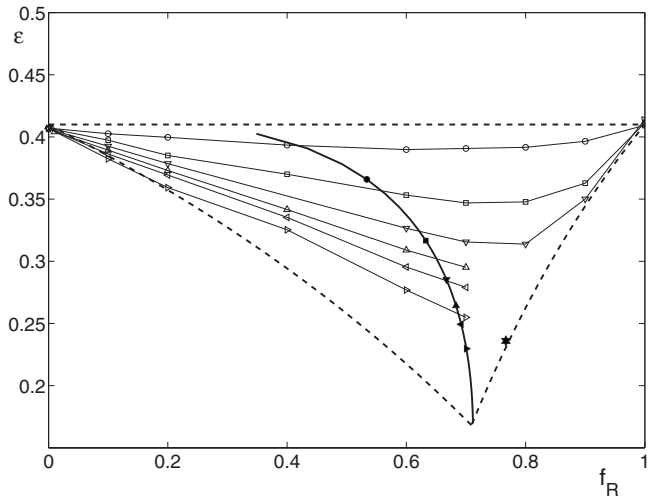

FIG. 4. Porosity of bidisperse packings as a function of the volume fraction of the larger grains. The packing characteristics are given in Table I. From top to bottom, data are for $\rho=2$ (○), 3 (□), 4 (▽), 5 (△), 6 (◁), and 8 (▷). The two lower dotted lines correspond to Eqs. (24) and (25). The thick solid line corresponds to the variations of the minimal porosity for various values of ρ provided by Eqs. (26) and (27); the dots on this curve provide the value of ρ. The star corresponds to the bottom layer of a bed with $\rho=8$ and $f_R \geq 0.8$ (see Fig. 5).

$$K = \frac{\Lambda^2}{8F}, \tag{18}$$

where F is the formation factor. This was recently confirmed by systematic calculations of [13], where K, F, and Λ were computed for a variety of porous media. Moreover, [13] showed that Λ is indeed approximately equal to twice the inverse of the surface-to-volume ratio,

$$\Lambda \approx 2\frac{V_p}{S_p}. \tag{19}$$

IV. GEOMETRIC PROPERTIES

Let us focus our discussion on the porosity of the bidisperse and log-normal packings which were defined in Sec. II B.

A. Bidisperse packings

The porosity of bidisperse packings is displayed in Fig. 4. First, it should be noted that the porosity of monodisperse packings ϵ_m is given by

$$\epsilon_m \approx 0.41, \tag{20}$$

in agreement with [12]. For bidisperse packings, the general physical effect is clear. If ρ is close to 1, the porosity variations are very small; in the opposite case, they may be quite large with a minimum that is located around $f_R=0.70$; f_R is recalled to be the volume fraction of large grains. The general shape of these curves is in agreement with the data that can be found in the literature (see [16] for instance); a more precise comparison will be done at the end of this section. The curves are seen to be incomplete in Fig. 4. This is due to the so-called segregation effect, which occurs for $\rho \geq 5$. The small particles tend to accumulate at the bottom of the packing where they entirely fill the void space between the large particles.

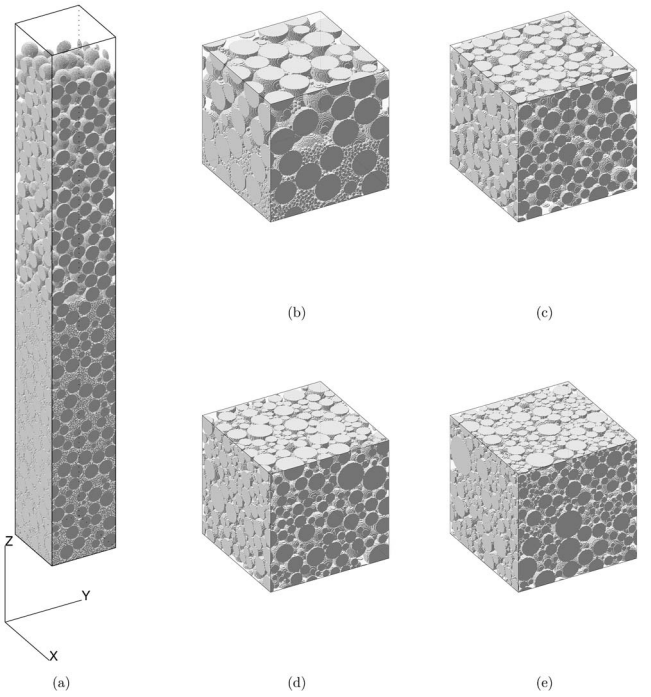

FIG. 5. (a) Illustration of the segregation effect for a bidisperse packing with a ratio $\rho=8$ and $f_R=0.85$. (b) is an enlarged view of the middle part of (a). Log-normal packings with $\sigma=0.2$ (c), 0.4 (d), and 0.6 (e).

Such an effect is illustrated in Figs. 5(a) and 5(b). The packing is actually composed of two parts. The upper part is almost exclusively composed by large particles while the lower one is progressively filled by small particles. Because of the imposed proportion between large and small particles, the upper front advances faster than the lower front, where the smaller particles fill in the gap. In the lower part of the packing, it is obvious that the volumetric proportion of large particles is different from the value f_R which is imposed.

The value f_{Ro} of f_R in the lower part of the packing can be estimated in the following approximate way in a binary mixture with an extreme size ratio $\rho \ll 1$. For an overall volume equal to 1, the large particles fill a volume $1-\epsilon_m$. The small particles fill the complement to 1, i.e., ϵ_m. The volume of the small particles is equal to $\epsilon_m\ (1-\epsilon_m)$. Therefore, f_{Ro} can be expressed as

$$f_{Ro} = \frac{1}{1+\epsilon_m} \tag{21}$$

which is about 0.71 for $\epsilon_m=0.41$. This situation corresponds to the maximal compaction for a binary mixture. The porosity in the lower part of the packing is simply ϵ_m^2. These simple properties are seen to be independent of the size ratio ρ provided that it is small.

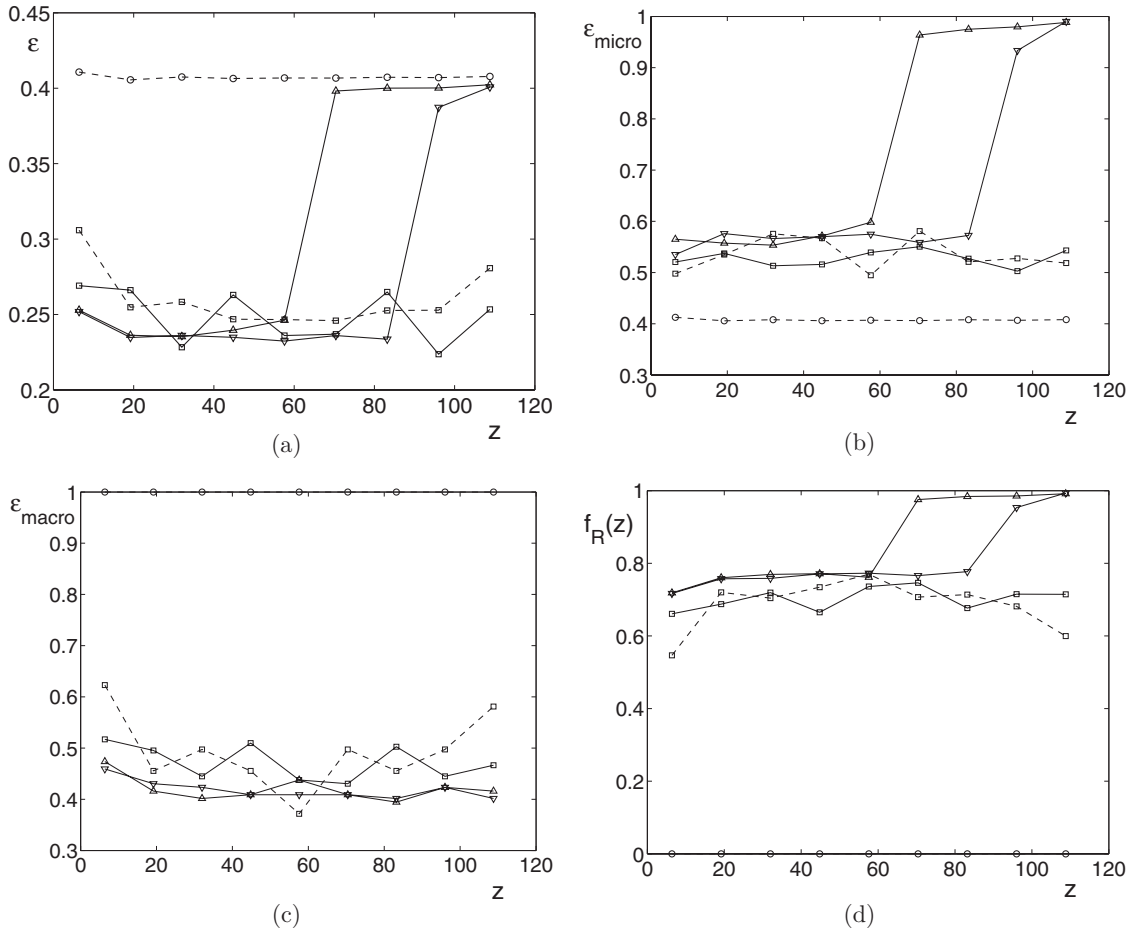

FIG. 6. Segregation effects in a bidisperse packing with $\rho=8$. Porosities are displayed as functions of the altitude z measured from the bottom of the box. They are obtained by averaging over slices of height 12.5. Data are for $f_R=0$ (dotted line, ○, $r=0.4$, $R=3.2$), 0.7 (dotted line, □; $r=0.4$, $R=3.2$), 0.7 (solid line, □, $r=0.22$, $R=1.78$), 0.8 (solid line, ▽, $r=0.22$, $R=1.78$), 0.85 (solid line, △, $r=0.22$, $R=1.78$). (a) Total porosity, (b) microporosity, and (c) macroporosity. The proportion of large grains f_R determined from the grain list is displayed in (d).

In the same way, one can estimate the heights H and h of the fronts of the large and small particles, respectively. The ratio between the numbers N and n of large and small particles in the packing can be derived from f_R and ρ:

$$\frac{n}{N}=\rho^3\frac{1-f_R}{f_R}. \tag{22}$$

Let us consider a packing whose basis has an area S. It is an easy matter to derive the height H of the packing composed only of the large particles. Then, the small particles are assumed to fill in the gaps in between these large particles; for the sake of simplicity, consider that the packing of the small particles inside the large voids is always equal to ϵ_m. It is easy to obtain

$$\frac{h}{H}=\frac{n}{N}\frac{1}{\rho^3\epsilon_m}=\frac{1-f_R}{\epsilon_m f_R}. \tag{23}$$

In Fig. 5(a), the ratio h/H can be approximated as 0.53. An immediate application of the previous equation yields $h/H=0.43$ for $\rho=8$ and $f_R=0.85$. The agreement is acceptable considering the simplicity of the argument. The discrepancy simply indicates that the porosity of the small particles inside the large pores is slightly larger than ϵ_m even for a ratio equal to 8.

One can go a little further in this direction and derive the shapes of the envelopes which are seen in Fig. 4. If the proportion of large grains is smaller than f_{Ro}, they are dispersed within a bed of small ones and the porosity is

$$\epsilon=\frac{(1-f_R)\epsilon_m}{1-f_R\epsilon_m}\geq\epsilon_m^2. \tag{24}$$

Conversely, if the population of large grains is larger, the amount of small ones is insufficient to fill the macropores. The porosity can be formally expressed as

$$\epsilon=\frac{f_R-1+\epsilon_m}{f_R}. \tag{25}$$

These two curves are illustrated in Fig. 4.

Let us now consider the various porosities that can be defined in the packing. The macroporosity is defined as the proportion of space between the large grains, and the microporosity as the proportion of space between the small grains. These quantities are illustrated in Fig. 6 for a radius ratio $\rho=8$. Averages are taken on slices of dimensions 16

$\times 16 \times 12.8$. The macroporosity is indeed found equal to ϵ_m; since the small grains fall down to the bottom of the bed, they have no influence on the arrangement of the large ones. However, the microporosity is larger because finite-sized grains cannot fill the macropores efficiently.

Segregation occurs only for the two largest values of f_R =0.8 and 0.85. In these two cases, compact bottom layers with identical characteristics develop; they differ only in their thicknesses. For f_R=0.7, the segregation effect disappears and the macroporosity is larger than ϵ_m because the presence of small grains prevents the large ones from forming a stable packing by themselves. The mixture composition is equal to the mean value throughout the bed thickness.

After these illustrations relative to segregation, it is useful to come back to Fig. 4. Reference [15] summarized previous experimental results and gave the variations of the minimum of porosity for each radius ratio ρ if $\rho \leq 0.741$:

$$\epsilon_{\min} = \epsilon_m - \epsilon_m(1-\epsilon_m)(1-2.35\rho+1.35\rho^2). \quad (26)$$

The other situation $\rho > 0.741$ is not used in this paper. The fractional volume v_R for which this minimum occurs is given by

$$v_R = \frac{1-\rho^2}{1+\epsilon_m}. \quad (27)$$

This quantity is displayed in Fig. 4. It does not agree well with our numerical data because the numerical packings are loose while the experimental systems are closely packed. Our data correspond to packings generated under the action of gravity without any further rearrangement in order to decrease the porosity. It is useful to note that for large values of ρ, when segregation occurs, some numerical experiments were performed; packings of large particles were built first and the small particles were dropped later; the results were the same as when large and small particles were dropped together. Therefore, the packings that were generated and their macroscopic transport properties are not well representative of closely packed beds; it will be seen later how the macroscopic properties of these closely packed beds can be obtained.

B. Log-normal packings

Examples of log-normal packings are provided in Figs. 5(c)–5(e), for σ=0.2, 04, and 0.6. The ratio $R_H/\tilde{R}$ is displayed in Fig. 3 together with the data relative to bidisperse packings. It is clearly seen that the values $R_H/\tilde{R}$ for the log-normal packings and the bidisperse packings with radius ratios equal to 2 and 3 are very close.

The porosities of the log-normal packings are displayed in Fig. 7 for various values of the standard deviation σ of the log-normal law (3). ϵ is a decreasing function of σ. The decrease is relatively slow at the beginning since ϵ is still equal to 0.4 for σ=0.2. Then, the decrease is more rapid, and almost a linear function of σ.

V. TRANSPORT PROPERTIES

This section is devoted to the study of conductivity and permeability of packings.

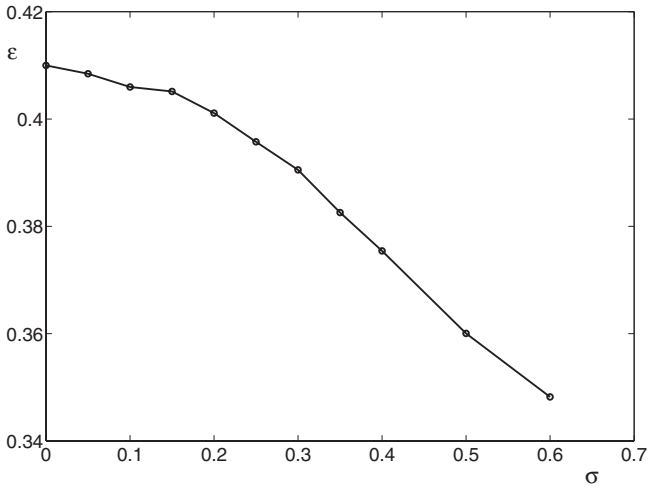

FIG. 7. Porosity of log-normal packings as a function of the standard deviation of the log-normal law (3).

A. Conductivity

1. Bidisperse packings

Systematic calculations were performed for the bidisperse packings previously discussed in Sec. II B. The first results are displayed in Fig. 8(a) and they show that overall the conductivity variations are similar to the porosity variations displayed in Fig. 4. However, the present figure has a very undesirable feature, namely, the two extreme values obtained for the monodisperse packings do not coincide. This is in contradiction with the fact that the macroscopic conductivity of a porous medium does not depend on the scale of the medium; for instance, if all the dimensions are multiplied by a factor 2, Σ should remain the same. Moreover, the porosities of these extreme monodisperse packings are very close to one another in Fig. 4; ϵ is equal to 0.407 and 0.409 for f_R=0 and 1, respectively. Therefore, the major cause of discrepancy between the extreme conductivities can only be the discretization effect since the ratio between the radii and the mesh size is not the same.

Therefore, a systematic study of discretization effects was started. Four discretizations were used for each sample, namely, N_c=128, 160, 192, and 256. Some results are reported in Fig. 8(b). They clearly show that the calculated conductivity Σ_{cal} is a linear function of the mesh size a/R_H. Moreover, Σ_{cal} can be easily extrapolated for a vanishing mesh size. Let us denote by Σ_∞ this value corresponding to a/R_H=0. The linear relation can be represented as

$$\Sigma_{\text{cal}} = \Sigma_\infty\left(1-\hat{S}\frac{a}{R_H}\right), \quad (28)$$

where the constant $\hat{S}$ depends *a priori* on the particular packing.

It turns out, as demonstrated by Fig. 8(c), that $\Sigma_{\text{cal}}/\Sigma_\infty$ is a function only of the mesh size a/R_H, and that it does not depend on the particular packings under consideration. The coefficient $\hat{S}$ is determined by a linear regression fit over all the numerical results:

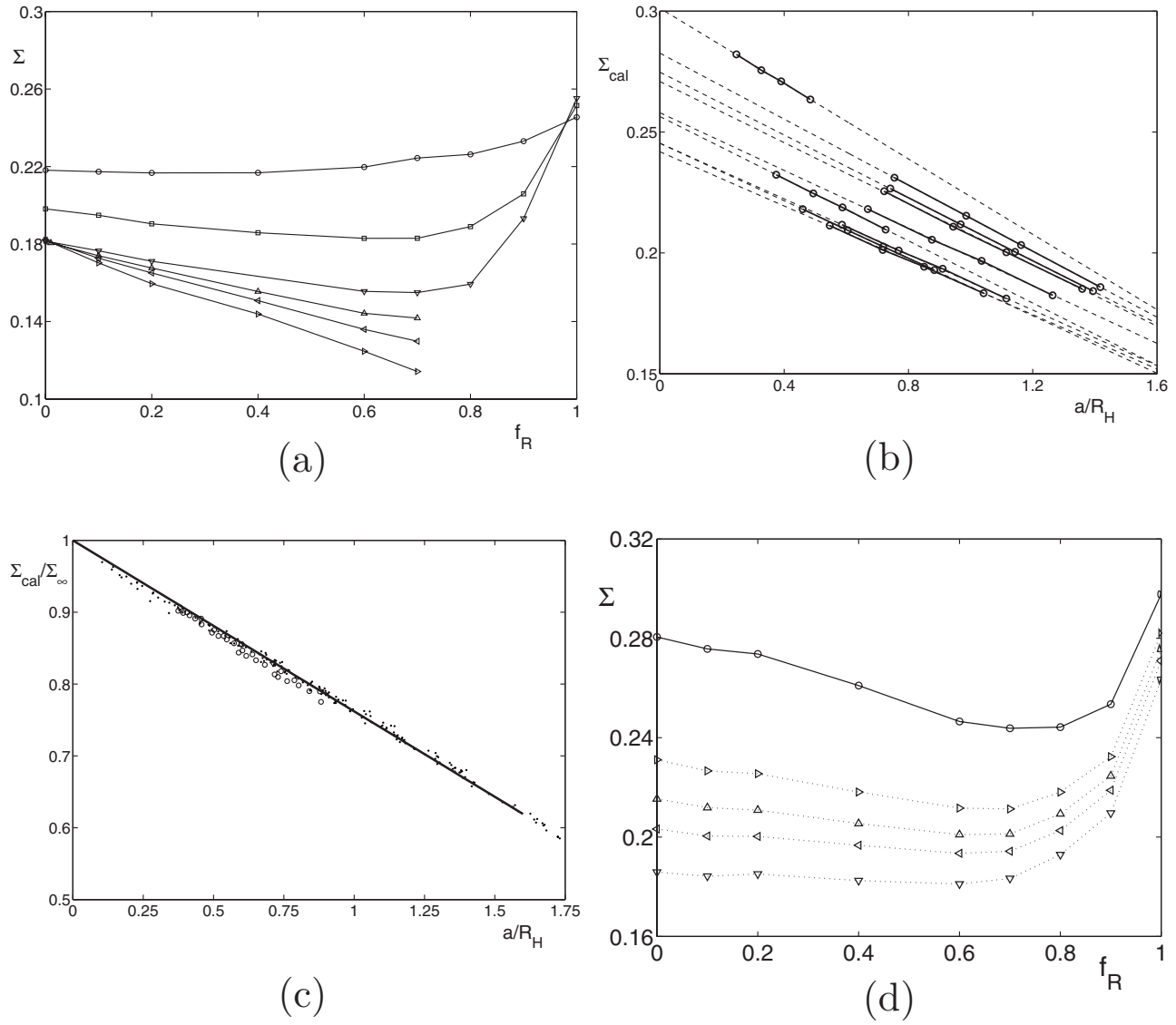

FIG. 8. Extrapolation of the conductivities. (a) Conductivities of bidisperse packings of spheres as a function of the volume fraction f_R of the larger grains; the packing characteristics are given in Table I; data from top to bottom are for $\rho=2$ (○), 3 (□), 4 (▽), 5 (△), 6 (◁), and 8 (▷). (b) Calculated conductivity Σ_{cal} for various bidisperse packings as a function of the mesh size a/R_H. (c) $\Sigma_{\mathrm{cal}}/\Sigma_\infty$ as a function of a/R_H for the various bidisperse packings (●) and log-normal packings (○). (d) Σ_{cal} and Σ_∞ (solid line) for bidisperse packings obtained with $\rho=3$; data from bottom to top are for $N_c=128$, 160, 192, and 256.

$$\hat{S} = 0.238. \tag{29}$$

This fit is really excellent and all the numerical results lie within −1.74% and +0.66% of the regression line.

Equation (28) can now be used in a systematic way in order to determine the extrapolated values Σ_∞ for each bidisperse packing. This process is illustrated in Fig. 8(d) for a particular value $\rho=3$. Note that the data in this sample are for a single slice. Hence, the results for $f_R=0$ and 1 are still slightly different because they correspond to different realizations of monodisperse packings. This is eliminated by taking statistical averages as seen below.

Then this extrapolation procedure is systematically applied to all the data displayed in Fig. 8(a) and the results are shown in Fig. 9(a). The differences due to the extrapolation procedure are important. It is seen that now the two extreme conductivities for monodisperse packings are identical in agreement with first principles.

2. Log-normal packings

The same procedure was followed to determine the macroscopic conductivity of the log-normal packings. Figure 8(c) shows that the conductivity of the log-normal packings follows the same relation (28) as the bidisperse packings which is quite a remarkable property. Thanks to this property, data for log-normal packings are extrapolated to a vanishing mesh size and the data are displayed in Fig. 9(b).

3. Overall correlations for conductivity

It is customary to represent the data according to the widely used Archie law ([29])

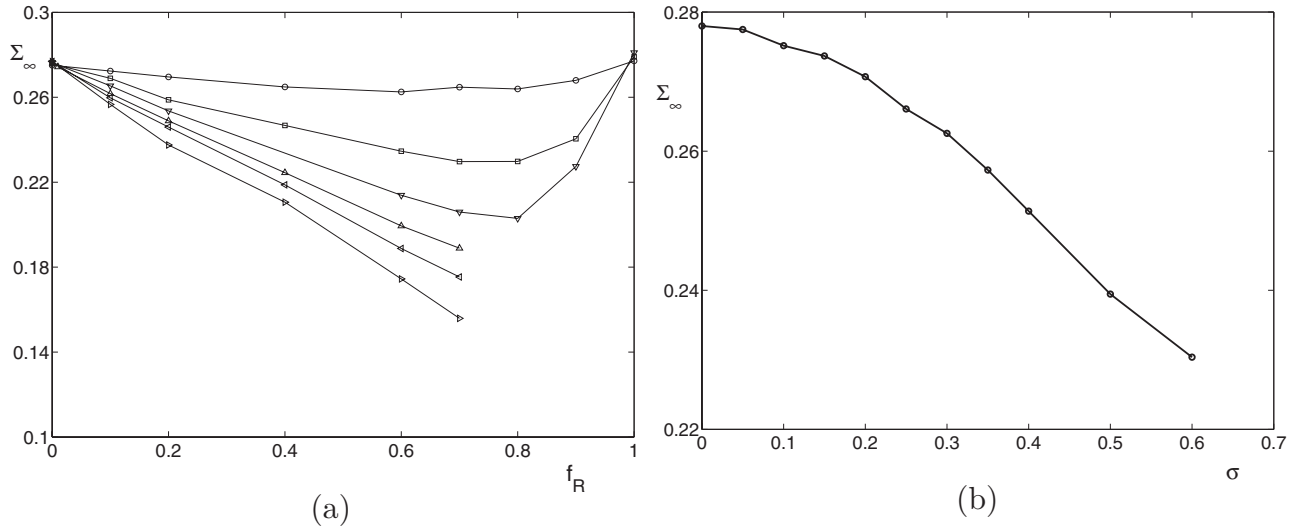

FIG. 9. Extrapolated conductivity Σ_∞. (a) Bidisperse packings: Σ_∞ as a function of the volume fraction of the larger grains f_R; data are for $\rho=2$ (○), 3 (□), 4 (▽), 5 (△), 6 (◁), and 8 (▷). (b) Log-normal packings: Σ_∞ as a function of the standard deviation σ.

$$\Sigma = \alpha\epsilon^m, \tag{30}$$

where the exponent m is the so-called cementation exponent. It has been measured by several authors on different types of material. Reference [30] obtained $m=1.64$ and $\alpha=0.80$ for Fontainebleau sandstones in the range 0.05–0.30. Reference [31] also observed a power law for sintered glass beads, with m equal to 1.6 for $0.1 \leq \epsilon \leq 0.40$. Her results are somewhat scattered because of sample heterogeneities; her most homogeneous samples yield $m \approx 1.4$. The authors of [32], using their own data and those of [33] for fused glass beads, obtained $m \approx 2.3$, $\alpha \approx 3.3$ for $0.02 \leq \epsilon \leq 0.2$ and $m \approx 1.5$, $\alpha \approx 1$ for $0.2 \leq \epsilon \leq 0.4$. Reference [34] also obtained $m \approx 1.5$ for $\epsilon \approx 0.3$. Of course, the porosity variations in these media result generally from various degrees of consolidation by cementation (for sandstones) or by sintering (for beads). Therefore, results for low porosities cannot be directly extrapolated to looser unconsolidated packings.

Reference [12] obtained an overall correlation for their data with a poor discretization and without any extrapolation,

$$\Sigma = 0.88\epsilon^{1.72}. \tag{31}$$

The present data are represented as functions of porosity in Fig. 10(a). It is seen that they can be represented by Archie's law

$$\Sigma_\infty = 0.808\epsilon^{1.2}, \tag{32a}$$

or equivalently

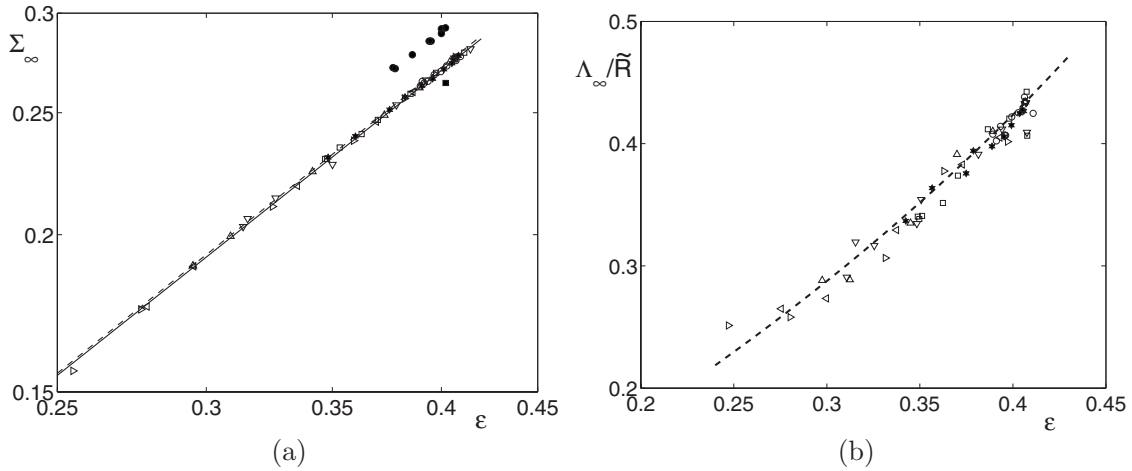

FIG. 10. (a) Extrapolated conductivity Σ_∞ as a function of porosity; the broken and solid lines correspond to (32a) and (32b), respectively; the black square dots correspond to the extrapolated data of [12] and the black circles to [35]. (b) Dimensionless length $\Lambda_\infty/\tilde{R}$ as a function of the porosity ϵ; the broken line corresponds to Eq. (34). In (a) and (b), the symbols correspond to bidisperse packings with $f_R=0$ to 1 and $\rho=2$ (○), 3 (□), 4 (▽), 5 (△), 6 (◁), and 8 (▷), and to log-normal packings with σ up to 0.6 (★).

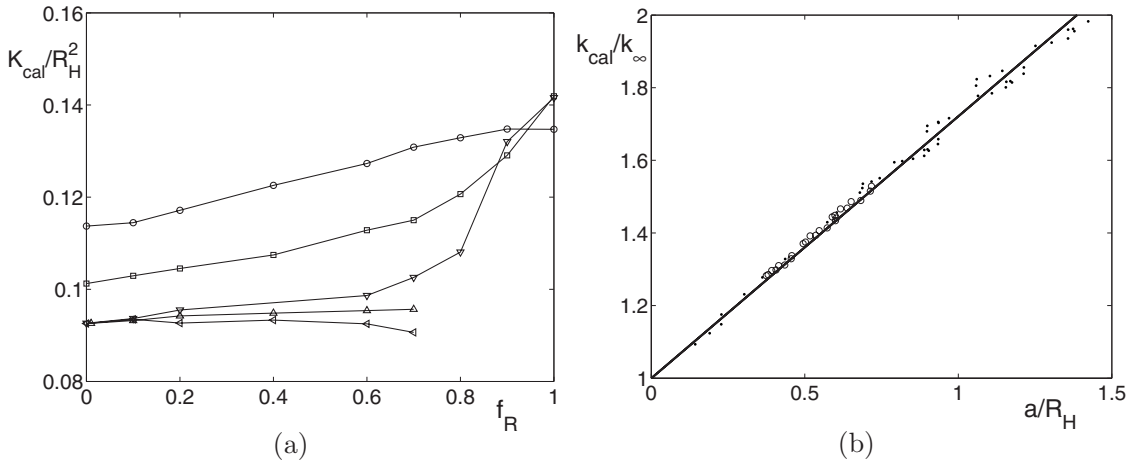

FIG. 11. (a) Dimensionless permeability K_{cal}/R_H^2 as a function of the volume fraction of the larger grains f_R for all the bidisperse packings; data are for $\rho=2$ (○), 3 (□), 4 (▽), 5 (△), and 6 (◁). (b) k_{cal}/k_∞ as a function of a/R_H for bidisperse packings with $\rho=2$, 4, and 6 (●) and for log-normal packings (○).

$$\Sigma_\infty = 0.772\epsilon - 0.038. \tag{32b}$$

These correlations are compared to the extrapolated value for spheres of [12] and to the experimental data of [35] for spheres.

Finally, the length scale Λ was systematically evaluated. Its numerical value depends again on the spatial discretization, but an extrapolated value Λ_∞ was obtained by considering finer and finer discretizations, as was done for the conductivity Σ. The convergence of Λ toward Λ_∞ always follows a linear law of the type of (28), but the convergence rate is not independent of the kind of size distribution, as it was for Σ [see Eq. (29)]. However, the discretization errors are also smaller than for Σ. The deviation of Λ from Λ_∞ never exceeds 7%, even for a/R_H larger than 3/2.

Note that the extrapolation is conducted in terms of Λ/R_H; hence, the influence of the discretization on the measure of R_H is also eliminated. The dimensionless ratio $(\Lambda/R_H)_\infty$ is found to depend on ϵ according to

$$\left(\frac{\Lambda}{R_H}\right)_\infty = 3.5 - 1.6\epsilon. \tag{33}$$

It is of the order of 3 in the range of porosity $0.25 \leq \epsilon \leq 0.42$. However, it should be remembered that R_H is evaluated from the discretized geometry, in which the interfacial area is overestimated by a factor which tends to 3/2 when the resolution parameter a/R_H tends to 0. Hence, Λ_∞ is indeed about twice the hydraulic radius as determined from the continuous geometry, in agreement with (19).

The combination of Eqs. (6) and (33), while taking the correction factor of 3/2 into account, yields

$$\frac{\Lambda_\infty}{\tilde{R}} = \frac{2\epsilon}{9(1-\epsilon)}(3.5 - 1.6\epsilon). \tag{34}$$

This expression is compared to the numerical data in Fig. 10(b) and seen to provide an estimate of Λ_∞ within a few percent for all the grain size distributions considered in the present work.

B. Permeability

1. Bidisperse packings

The same route was followed for permeability. First, the permeability was calculated systematically for all the packings and the results are displayed in Fig. 11(a). They are normalized by the square of the hydraulic radius. Despite this normalization, the same effect as before is visible for $f_R=0$ and 1, namely, the corresponding dimensionless permeabilities are different for these two monodisperse packings which differ only in the size of the spheres; note that the porosity is almost exactly the same as can be seen in Fig. 4. Again, this is probably due to discretization effects since the permeability of monodisperse packings should be proportional to the square of the sphere radii.

This influence of discretization was studied by the same technique as in Sec. V A 1 with four values of $N_c=128$, 160, 192, and 256. Let K_{cal} denote the numerical permeability for a given discretisation a/R_H. However, when the ratio $K_{cal}/R_H^2/(K/R_H^2)_\infty$ is displayed as a function of a/R_H (in exact analogy with what was done in Fig. 8), the data are not well gathered by this representation. Another representation was derived from the classical Carman-Kozeny equation [36]

$$K = \frac{\epsilon R_H^2}{k}, \tag{35a}$$

where k is called the Kozeny constant; it is supposed to be of the order of a few units and almost constant for a large variety of conditions. This relation can be transposed for the numerical values as

$$K_{cal} = \frac{\epsilon R_H^2}{k_{cal}}. \tag{35b}$$

Therefore, it was logical to try to display the results through the corresponding values of k_{cal},

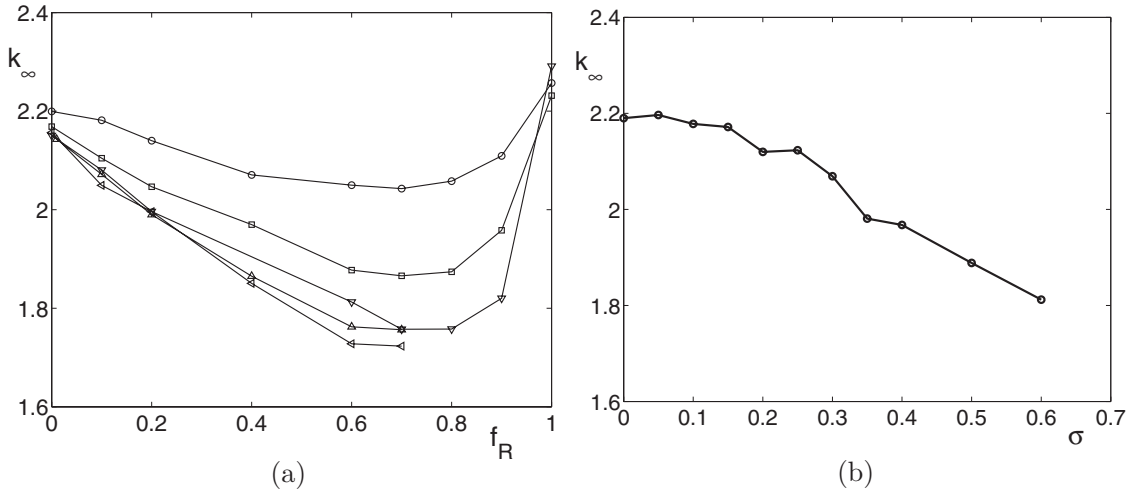

FIG. 12. Extrapolated Kozeny constant k_∞. (a) Bidisperse packings: k_∞ as a function of the volume fraction of the larger grains f_R; data are for ρ=2 (○), 3 (□), 4 (▽), 5 (△), and 6 (◁). (b) Log-normal packings: k_∞ as a function of the standard deviation σ.

$$\frac{k_{\mathrm{cal}}}{k_\infty} = 1 + \hat{S}_k \frac{a}{R_H}, \tag{36}$$

where $\hat{S}_k$ is a constant. In Fig. 11(b), the data follow a single line as was the case for conductivity in Fig. 8(c). The constant $\hat{S}_k$ can be calculated by means of a linear regression fit,

$$\hat{S}_k = 0.7212. \tag{37}$$

Finally, the extrapolated Kozeny constant is displayed in Fig. 12(a) for all the bidisperse packings. Two features are worth noticing. First, k_∞ has almost the same value for f_R equal to 0 and 1. The differences are reduced to a few percent: k_∞ varies between 2.1 and 2.2 for f_R=0, and between 2.22 and 2.3 for f_R=1. This is due to the fact that the differences in porosity and wetted surface are taken into account, and therefore eliminated, in k and not in K. Second, k_∞ is almost the same for ρ equal to 5 and 6.

2. Log-normal packings

The same procedure was followed to determine the macroscopic permeability of the log-normal packings. As for conductivity, the permeability of log-normal packings is seen in Fig. 11(b) to follow (36). Therefore, the same procedure can be followed to extrapolate the Kozeny constant, and the results are displayed in Fig. 12(b) as a function of the standard deviation. It is interesting to notice that the Kozeny constant is almost a linear function of σ. Moreover, its variations are somewhat limited around 2.

3. Overall correlations for permeability

Various representations can be proposed to gather the previous results. They are given for the sake of completeness. $(K/R_H^2)_\infty$ is displayed in Fig. 13 for the two types of studied packings as a function of the geometric characteristics f_R and σ. It is seen to be reasonably constant for these sets of parameters,

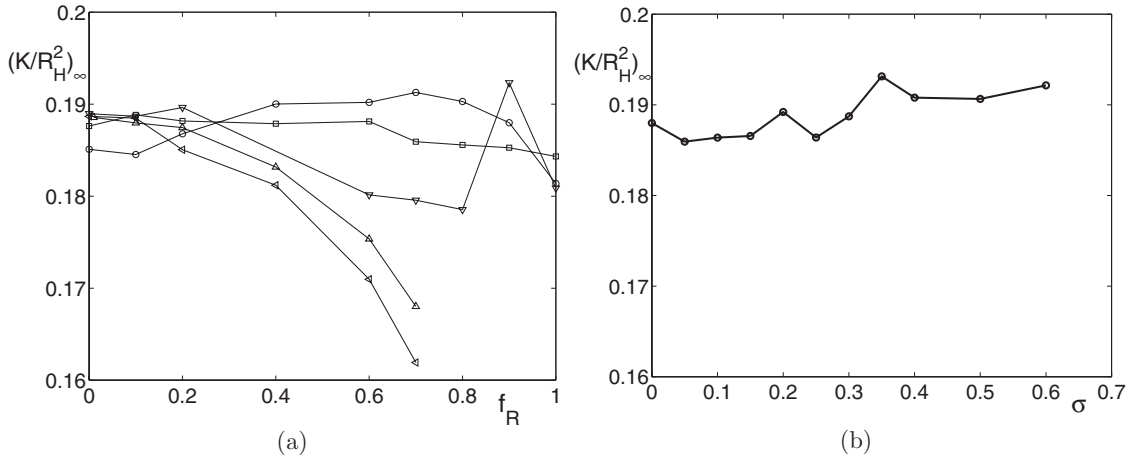

FIG. 13. Dimensionless extrapolated permeability $(K/R_H^2)_\infty$ as a function of the volume fraction of the larger grains f_R for all the bidisperse packings (a), and as a function of the standard deviation σ for the log-normal packings (b). Data in (a) are for ρ=2 (○), 3 (□), 4 (▽), 5 (△), and 6 (◁).

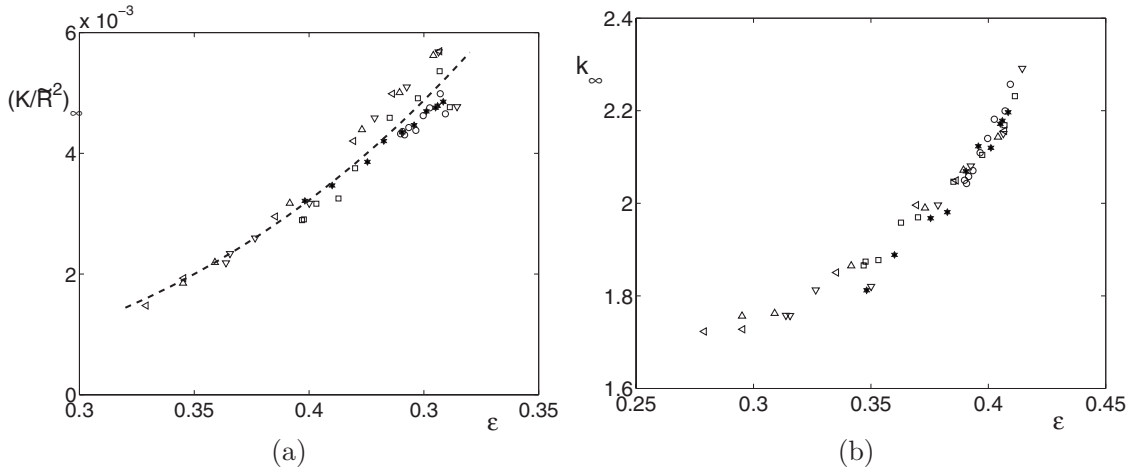

FIG. 14. (a) Dimensionless permeability $(K/\tilde{R}^2)_\infty$ as a function of porosity; the broken line is Eq. (39). (b) Extrapolated Kozeny constant k_∞ as a function of the porosity ϵ. In (a) and (b), the symbols correspond to bidisperse packings with f_R=0 to 1 and ρ=2 (○), 3 (□), 4 (▽), 5 (△), and 6 (◁), and to log-normal packings with σ up to 0.6 (★).

$$0.162 \leq \left(\frac{K}{R_H^2}\right)_\infty \leq 0.195. \tag{38}$$

Note again that, by extrapolating the ratio K/R_H^2, the influence of the discretization on the measure of R_H is eliminated. Permeabilities can also be displayed as functions of porosity. Permeabilities can be made dimensionless either by the square hydraulic radius R_H^2 or by the equivalent radius $\tilde{R}^2$ [cf. (5)]. First, the trend for $(K/R_H^2)_\infty$ is complex and its interpretation is not obvious. Second, the trend displayed in Fig. 14(a) is much simpler and it can be summarized by a power law

$$\left(\frac{K}{\tilde{R}^2}\right)_\infty = 0.0835\epsilon^{3.1}. \tag{39}$$

The most successful formulation for unifying the numerical results is in terms of the Kozeny constant, as shown in Fig. 14(b), where k_∞ is plotted as a function of ϵ. It is observed that, for all the packings investigated here, k_∞ is about 2 within at most $\pm 15\%$.

4. Overall conductivity-permeability correlations

Finally, the plot of the ratio KF/R_H^2 in Fig. 15(a) clearly shows that the permeability and conductivity coefficients are strongly correlated. The data for all the bidisperse and log-normal packings considered in the foregoing fall onto a single curve, which can be represented by the heuristic formula

$$\frac{KF}{R_H^2} = \frac{1 - 1.88\epsilon}{(1-\epsilon)^2}. \tag{40}$$

Λ can also be used instead of R_H. The ratio $(KF/\Lambda^2)_\infty$ is plotted in Fig. 15(b) as a function of ϵ. It is found nearly constant, when ϵ is in the investigated interval $0.25 \leq \epsilon \leq 0.41$, and comprised between 1/8 and 1/12 in agreement with (18). Its residual dependence on porosity can be de-

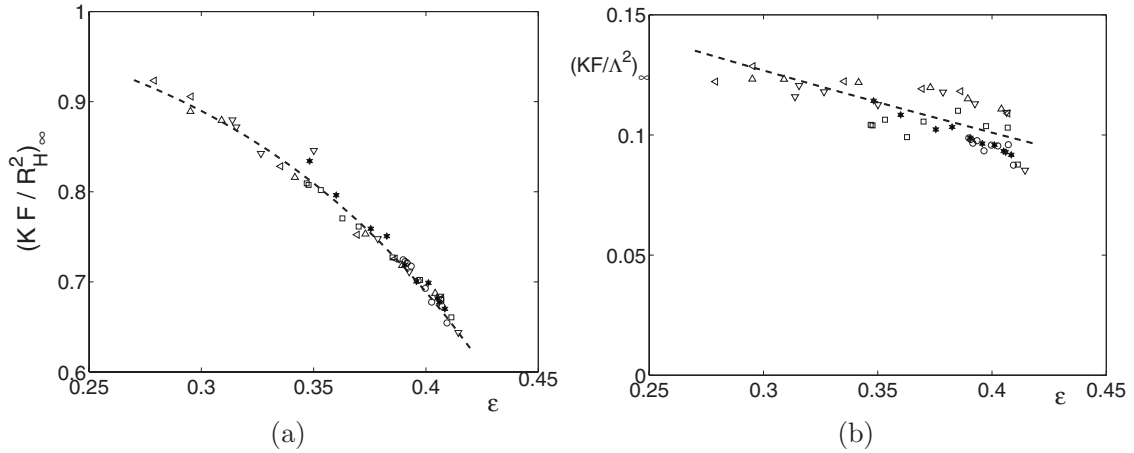

FIG. 15. Ratios $(KF/R_H^2)_\infty$ (a) and $(KF/\Lambda^2)_\infty$ (b) as functions of the porosity ϵ. In (a), the broken line corresponds to Eq. (40); in (b), the broken line corresponds to the combination of Eqs. (32), (34), and (39). In (a) and (b), the symbols correspond to bidisperse packings with f_R=0 to 1 and ρ=2 (○), 3 (□), 4 (▽), 5 (△), and 6 (◁), and to log-normal packings with σ up to 0.6 (★).

scribed within ±15% by the combination of Eqs. (32), (34), and (39), which is nearly equivalent in this range of porosity to the linear expression

$$\frac{KF}{\Lambda^2} = 0.2 - \epsilon/4. \tag{41}$$

VI. CONCLUDING REMARKS

The study reported in [12] has been extended to polydisperse packings. Bidisperse and log-normal packings were systematically generated. Because of the random sequential algorithm which is used and which simulates deposition under gravity, the packings are loose. Their macroscopic geometric and transport properties were calculated.

The numerical porosity has the same general variations with the proportion of large spheres as obtained either experimentally or numerically by others. There exists a minimum for each radius ratio. However, the numerical porosity corresponds to a loose packing.

Discretization effects which were shown to be important were analyzed and extrapolation formulas are proposed for the conductivity and permeability for bidisperse and log-normal packings. A way to minimize these effects would be to use unstructured meshes with a tetrahedral decomposition of space as was started in [37].

Finally, the results are displayed as functions of porosity. Power laws are obtained for the conductivity [see (32)] and for the permeability [see (39)]. The length scale Λ is also successfully represented as a function of the porosity (34). In addition, the Kozeny constant and the ratio $\frac{KF}{\Lambda^2}$ are found to be nearly independent of the porosity, whatever the grain size distribution. These relations are likely to be useful to extrapolate the results obtained for loose packings to closely packed systems.

ACKNOWLEDGMENTS

This work was partly supported by a grant from the Institut Francais du Pétrole and most computations were performed at CINES (Montpellier), subsidized by the MENESR, whose support is gratefully acknowledged.

[1] J. G. Berryman, Phys. Rev. A **27**, 1053 (1983).
[2] R. M. German, *Particle Packing Characteristics* (Metal Powder Industry Federation, Princetown, 1989).
[3] J. L. Chermant, *Caractérisation des Poudres et des Céramiques* (Hermes, Paris, 1993).
[4] P. Meakin and A. T. Skjeltrop, Adv. Phys. **42**, 1 (1993).
[5] G. C. Barker, in *Granular Matter—An Interdisciplinary Approach*, edited by A. Mehta (Springer-Verlag, Berlin, 1993).
[6] A. S. Clarke and J. D. Wiley, Phys. Rev. B **35**, 7350 (1987).
[7] A. Yang, C. T. Miller, and L. D. Turcoliver, Phys. Rev. E **53**, 1516 (1996).
[8] D. He, N. N. Ekere, and L. Cai, Phys. Rev. E **60**, 7098 (1999).
[9] A. R. Kansal, S. Torquato, and F. H. Stillinger, J. Chem. Phys. **117**, 8212 (2002).
[10] K. L. Kristiansen, A. Woutersee, and A. Philipse, Physica A **358**, 249 (2005).
[11] M. J. Vold, J. Phys. Chem. **64**, 1616 (1960).
[12] D. Coelho, J.-F. Thovert, and P. M. Adler, Phys. Rev. E **55**, 1959 (1997).
[13] A. M. Valfouskaya, P. M. Adler, J.-F. Thovert, and M. Fleury, J. Appl. Phys. **97**, 083510 (2005).
[14] E. Santiso and E. A. Müller, Mol. Phys. **100**, 2461 (2002).
[15] A. B. Yu and N. Standish, Powder Technol. **52**, 233 (1987).
[16] A. B. Yu and N. Standish, Powder Technol. **55**, 171 (1988).
[17] S. A. Patlazhan, Physica A **198**, 368 (1993).
[18] D. M. E. Thies-Weesie and A. P. Philipse, J. Colloid Interface Sci. **162**, 470 (1994).
[19] H. Freund, T. Zeiser, F. Huber, E. Klemm, G. Brenner, F. Durst, and G. Emig, Chem. Eng. Sci. **58**, 903 (2003).
[20] Y. L. Ding, Z. L. Wang, D. S. Wen, and M. Ghadiri, Powder Technol. **153**, 13 (2005).
[21] J. M. P. Q. Delgado, Heat Mass Transfer **42**, 279 (2006).
[22] D. Mehta and M. C. Hawley, Ind. Eng. Chem. Process Des. Dev. **8**, 280 (1969).
[23] P. M. Adler, *Porous Media: Geometry and Transport* (Butterworth/Heinemann, Stoneham, MA, 1992).
[24] J. F. Thovert, F. Wary, and P. M. Adler, J. Appl. Phys. **68**, 3872 (1990).
[25] D. L. Johnson, J. Koplik, and L. M. Schwartz, Phys. Rev. Lett. **57**, 2564 (1986).
[26] R. Lemaître and P. M. Adler, Transp. Porous Media **5**, 325 (1990).
[27] R. Peyret and T. D. Taylor, *Computational Methods for Fluid Flow*, Springer Series in Computational Physics (Springer-Verlag, Berlin, 1985).
[28] D. B. Pengra, S. Li, S. X. Li, and P. Z. Wong, in *Dynamics in Small Confining Systems II*, edited by J. M. Drake, J. Klafter, K. Kopelman, and S. M. Troian, MRS Symposia Proceedings No. 366 (Materials Research Society, Pittsburgh, 1995).
[29] G. E. Archie, Trans. AIME **146**, 54 (1942).
[30] C.G. Jacquin, Rev. Inst. Fr. Pet. Ann. Combust. Liq. **19**, 921 (1964).
[31] D. Guillot, Ph.D. thesis, ENSM, Paris, 1982.
[32] P.-Z. Wong, J. Koplik, and J. P. Tomanic, Phys. Rev. B **30**, 6606 (1984).
[33] D. L. Johnson, T. J. Plona, C. Scala, F. Pasierb, and H. Kojima, Phys. Rev. Lett. **49**, 1840 (1982).
[34] L. M. Schwartz, J. R. Banavar, and B. I. Halperin, Phys. Rev. B **40**, 9155 (1989).
[35] D. A. Robinson and S. P. Friedmann, Physica A **358**, 447 (2005).
[36] P. C. Carman, Trans. Inst. Chem. Eng. **15**, 150 (1937).
[37] I. Malinouskaya, I. Bogdanov, J.-F. Thovert, and P. M. Adler (unpublished).